

Radiative cooling dynamics of isolated N_2O^+ ions in a cryogenic electrostatic ion storage ringA. Hirota,^{1,2} R. Igosawa,^{1,2} N. Kimura^{1,2,*}, S. Kuma,² K. C. Chartkunchand², P. M. Mishra², M. Lindley^{2,3,†}, T. Yamaguchi¹, Y. Nakano^{2,4} and T. Azuma²¹*Department of Physics, Saitama University, Saitama 338-8570, Japan*²*Atomic, Molecular and Optical Physics Laboratory, RIKEN, Saitama 351-0198, Japan*³*Department of Materials and Life Sciences, Sophia University, Tokyo 102-8554, Japan*⁴*Department of Physics, Rikkyo University, Tokyo 171-8501, Japan*

(Received 21 May 2020; revised 13 July 2020; accepted 23 July 2020; published 26 August 2020)

We study radiative cooling processes of N_2O^+ ions isolated in vacuum by taking advantage of the extended storage times possible with a cryogenic electrostatic ion storage ring. The temporal evolution of the internal state populations of the N_2O^+ ions after being stored in the ring was state-selectively measured by action spectroscopy via a predissociation process using a wavelength-tunable pulsed laser. The rotational level population remained unchanged up to about 200 s after ion storage, which is consistent with theoretical predictions and the small permanent dipole moment. On the other hand, we found that depletion of the vibrational excited states in the NN-O stretching mode proceeded within 5 s, while a noticeable increase of the ground-state population was not observed. This implies that the initial populations of the vibrational excited states are relatively small. We discuss such behavior in the context of the initial population distribution of ions extracted from the ion source with a simulation based on simple cascade modeling.

DOI: [10.1103/PhysRevA.102.023119](https://doi.org/10.1103/PhysRevA.102.023119)**I. INTRODUCTION**

Excited molecular ions isolated in vacuum dissipate their internal energy solely via spontaneous emission. This radiative cooling (RC) is one of the fundamental processes in molecular science. The RC process involving multiple internal degrees of freedom (electronic, vibrational, and rotational) reflects molecular properties including the electronic structure and the molecular geometry. Understanding this process has been indispensable in studying slow unimolecular dissociation and controls the extent of thermalization of molecular ions in ion traps [1]. It is also essential in predicting the radiative properties of the constituent molecules of interstellar molecular clouds.

Historically, advanced experimental devices like ion traps and storage rings for confining and controlling ions in vacuum for sufficiently long times have enhanced both experimental and theoretical research of RC dynamics in molecules. Ion-beam storage devices in particular, with their ability to trace the temporal evolution of internal state conditions and excellent product detection efficiency, are ideal for observing very slow processes beyond the millisecond timescale [2]. For instance, H_3^+ , with its equilateral triangular structure, is a key species in the evolution of molecules in space. It has attracted much attention for a long period of time due to its very slow cooling rate coupled with the existence of highly excited forbidden rotational Rydberg states [3,4]. The cooling process and their initial condition in the ion source have been studied by Coulomb explosion measurements and dissociative

recombination (DR) imaging experiments at the Heidelberg Test Storage Ring (TSR) and the CRYRING storage ring at Manne Siegbahn Laboratory, Stockholm University. The DR processes of HD^+ in selected vibrational states were also studied in detail [5]. As an alternative approach, the observation of depletion of thermalized polyatomic molecular ions using wavelength-tunable pulsed lasers has provided the vibrational cooling rates of molecules kept isolated on the 100 ms timescale [6,7]. Although this approach did not reveal state-selected populations, the study has led to recent findings of inverse internal conversion followed by recurrent fluorescence, which plays a crucial role in the electronic cooling of a variety of molecules such as small carbon cluster anions (e.g., C_4^- , C_6^-) [8–10] and polycyclic aromatic hydrocarbon (PAH) cations (e.g., $\text{C}_{14}\text{H}_{10}^+$, $\text{C}_{10}\text{H}_8^+$) [11,12]. The observed electronic and vibrational RC behavior has been well described by statistical treatments based on the density of states and detailed balance theory [13], and the initial internal energy and its distribution have been important topics of discussion [14,15].

Recent developments of the cryogenic ion storage rings DESIREE [16], CSR [17], and RICE (Riken cryogenic electrostatic ion storage ring) [18] have realized far longer storage times, sometimes beyond hours, and have enabled the exploration of very slow RC processes. The temporal evolution of the internal energy of small carbon cluster anions and metal cluster anions involving vibrational RC was observed up to about 60 s storage time at DESIREE [19–21]. The rovibrational-state-selective observation of the RC processes of diatomic hydride molecular ions such as CH^+ , OH^- , and HeH^+ was demonstrated at CSR [22–24] and DESIREE [25]. These heteronuclear diatomic molecules have high rotational cooling rates due to large rotational constants and dipole

*Corresponding author: naoki.kimura@riken.jp

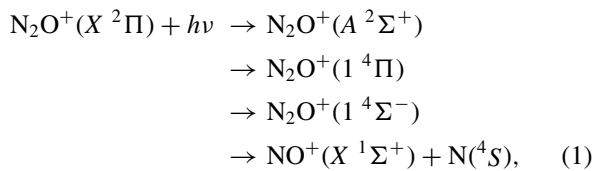
†Present address: Department of Chemistry, The University of Tokyo, Tokyo 113-8656, Japan.

moments, allowing rotational RC to the ground state to be accomplished within 1000 s ion storage time.

In this paper, we report on the RC process of a triatomic molecular ion observed with RICE. This possesses new challenges in the understanding of quantum systems with multiple vibrational degrees of freedom. In general, the rotational RC process of triatomic molecules is slow, due to small permanent dipole moments and rotational constants. Additionally, the increased complexity due to multiple vibrational and rotational modes and their mutual interactions makes the dynamics complicated. In spite of this, their cooling dynamics are still governed by the discrete level structure rather than the density of states. Here we employ the linear triatomic molecular ion N_2O^+ as the target of our study. Since N_2O^+ has a linear structure with a central N atom, it has two rotational degrees of freedom. For vibrations, there are three modes ($\nu_1 \nu_2 \nu_3$): a NN-O stretching (ν_1), a bending (ν_2), and a N-NO stretching (ν_3). A theoretical dipole moment of $-0.6933D$ was reported [26]. In contrast with H_3^+ , N_2O^+ is characterized by a lower degree of symmetry, which leads to allowed vibrational transitions and the decoupling of vibrational and rotational modes. We take advantage of this simple property of N_2O^+ to clarify the effect of the multimode nature of molecules on their RC behavior, which is our primary motivation for the present study. In addition, the level structures of N_2O^+ and the dissociation processes have been extensively investigated [26–50] because it is an intermediate product in the ion-molecular reaction $\text{O}^+ + \text{N}_2$, which is one of the most important reactions in Earth’s upper atmosphere [51,52]. The rovibrational population in the $X^2\Pi$ electronic ground state can be probed by UV photoexcitation spectroscopy to the predissociative $A^2\Sigma^+$ state, with experimental observations having been reported for supersonic-expanded [53,54] and buffer-gas-cooled [55] ions. Storing the N_2O^+ molecule in cryogenic ion storage rings enables the temporal evolution of its rovibrational population distribution to be traced in real-time over an extended time period.

II. EXPERIMENT

We observed time evolution of the internal state population of an N_2O^+ ion beam stored in RICE by the detection of neutral N produced by the active predissociation process



with tunable pulsed laser irradiation. The potential-energy curves of the N_2O^+ molecule are shown in Fig. 1. The ions in the $X^2\Pi$ electronic ground state are photoexcited to a specific vibrational level of the $A^2\Sigma^+$ electronic excited state. Through spin-orbit coupling with the $1^4\Pi$ state, they are transferred to the dissociative state $1^4\Sigma^-$ with a certain lifetime. It has also been proposed that another dissociation path opens via vibronic coupling with the $X^2\Pi$ state when the vibrational energy is high, as observed in photofragmentation spectroscopy [42,45,47]. A theoretical study by Meng *et al.* [46] proposed different dissociation mechanisms via $1^4\Sigma^-$,

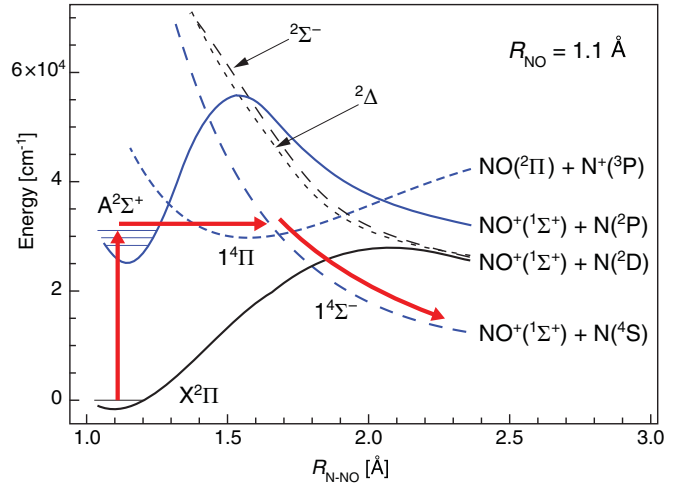


FIG. 1. The potential-energy curves of N_2O^+ as a function of the N-NO distance $R_{\text{N-NO}}$ in the N-N-O collinear dimension. Note that the vibrational transitions which we observe correspond to the NN-O stretching mode. The blue curves indicate the electronic states involved in the predissociation path shown by the arrows. Reproduced and modified from relevant literature [45].

not $1^4\Pi$, in both paths with bent structures. An additional path to $\text{N}(^2D)$ assuming the coupling to $2^2\Sigma^-/2^2\Delta$ via $1^4\Pi$ was proposed to explain the observations [45].

Figure 2 shows the schematic setup of the laser dissociation experiment with RICE. The detailed descriptions are given in Refs. [18,56]. N_2O^+ ions are produced in an electron cyclotron resonance (ECR) ion source (PANTECHNIK, Nanogan) under low rf power conditions. The hot N_2O^+ ions were injected into RICE as a 10 keV ion beam with a bunch width of 13 μs , which is in accordance with their circulation period in the ring. The ions are stored in RICE at cryogenic temperatures (≈ 4 K) and ultrahigh vacuum conditions [18], which enables long-period ion storage over 100 s. The typical number of stored ion were on the order of 10^5 – 10^6 at 1 s after injection.

The stored beam produced neutral species either by laser-induced predissociation or collisions with residual gas (mostly H_2) in the ring. We detect neutral N fragments by action spectroscopy and note that the different predissociation paths do not affect the results because the N fragments are detected regardless of the electronic state. These neutrals produced

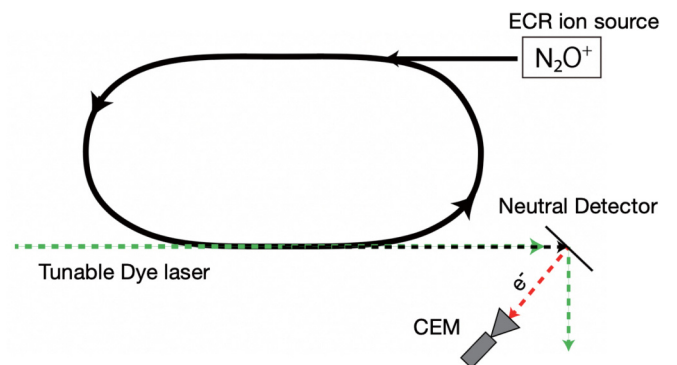


FIG. 2. Schematic overview of the present experimental setup.

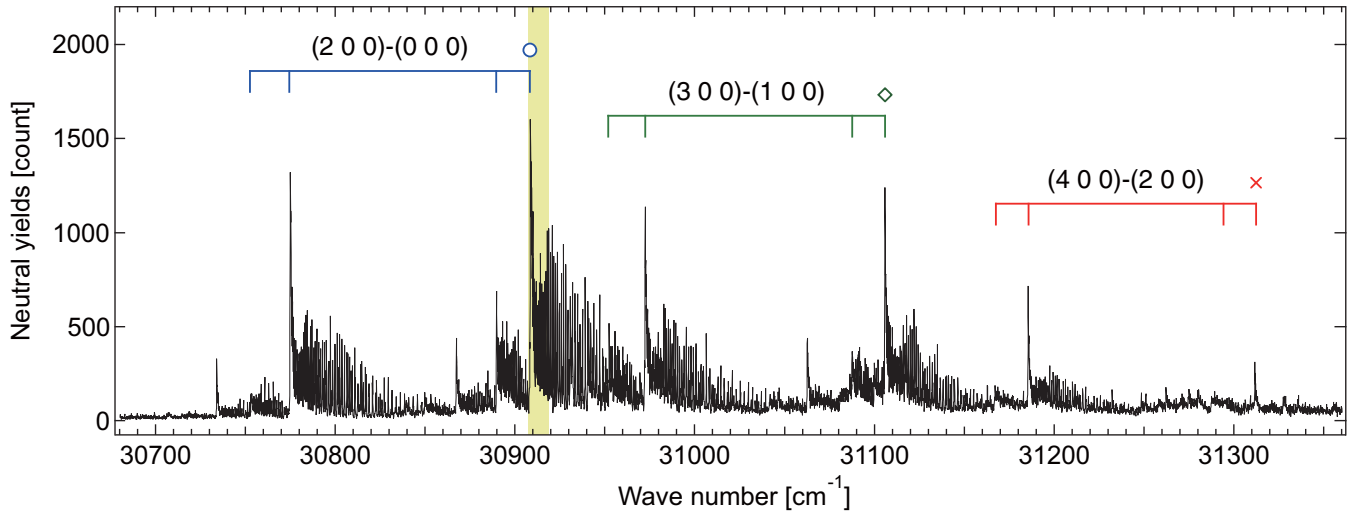


FIG. 3. $A^2\Sigma^+-X^2\Pi$ photodissociation spectrum of N_2O^+ measured at a storage time of 90 ms. The wavelength region corresponds to the $\Delta v_1 = 2$ sequence, with the main features attributed to the rotational bandheads of the $(v_1' 0 0)-(v_1'' 0 0)$ transitions. The filled yellow area represents the measured region of Fig. 4. By the circle, diamond, and cross symbols, we annotate the bandhead positions considered in Figs. 5 and 6.

in the straight section of RICE travel to the neutral particle detector placed at the extension of the straight section. The detector consists of a channel electron multiplier (CEM: SJUTS, KBL25RS) and an aluminum mirror. The neutral products impinge on the mirror surface, resulting in secondary electrons emitted from the mirror surface due to the 10 keV kinetic energy of the products. These secondary electrons are accelerated by a bias voltage of 500 V and detected by the CEM. The decay of beam intensity in the ring was continuously monitored by measuring the neutral yield due to collisions with the residual gas. The laser predissociation experiment was performed at different storage times up to 200 s for the rotational cooling study and up to 5 s for the vibrational cooling study. The laser system consists of a second-harmonic generator coupled to a dye laser (Sirah Cobra-Stretch, Exciton DCM/Ethanol dye mixture) pumped by the second harmonic of a Nd:YAG pulse laser (Cutting Edge Optics Gigashot at 100 Hz). The timing of laser irradiation was synchronized with the ion injection. For long-time storage measurements over 10 ms, we irradiated with a train of laser pulses by operating a mechanical shutter placed in front of a view port of the RICE chamber. The wavelength of the laser was monitored by a high-precision wavelength meter (High Finesse, WS6). To avoid saturation of the detector, we measured the laser-power dependence of the neutral yields and fixed the power to be lower than that which induced saturation at the most intense bandhead as the experimental condition. The power output of the dye laser was kept constant over the scanning region of 316–326 nm.

III. RESULTS AND DISCUSSION

A. Rovibrational spectroscopy and rotational radiative cooling dynamics

Figure 3 shows a photodissociation spectrum of N_2O^+ at a storage time of 90 ms. The neutral yield was accumulated over 50 repetitions of injection and dumping of the ion bunch.

The spectrum covers the $\Delta v_1 = v_1' - v_1'' = 2$ sequence of $A^2\Sigma^+-X^2\Pi$ transitions, where v_1' and v_1'' are the vibrational quantum numbers of the upper and lower states, respectively, in the NN-O stretching mode. The most intense features are assigned to the $(v_1' 0 0)-(v_1'' 0 0)$ bands. For each vibrational transition, four rotational bandheads are assigned to the P and Q branches of the transitions with the spin-orbit splitting in the ground state, $A^2\Sigma^+-X^2\Pi_{1/2}$ and $A^2\Sigma^+-X^2\Pi_{3/2}$. Due to the inverted spin-orbit parameter ($A'' = -132 \text{ cm}^{-1}$) in this state [35], the energy levels of $^2\Pi_{3/2}$ components are lower than $^2\Pi_{1/2}$, and the transitions from them to the common upper vibrational levels in the $A^2\Sigma^+$ state appear on the blue side of the spectrum.

We focused on the rotational structure in the vicinity of the main bandhead of $A^2\Sigma^+(2 0 0)-X^2\Pi_{3/2}(0 0 0)$, the filled area in Fig. 3, and investigated changes in their spectral shape during storage. The predissociation spectra were observed at a storage time of 9 ms and compared with a simulation using the PGOPHER [57] program in Fig. 4. The simulated spectra were fit to the experimental data by using the molecular constants and the rotational temperature as variable parameters. The observed spectrum was well reproduced by the simulation supposing a rotational temperature of $320(\pm 20)$ K [compare Figs. 4(a) and 4(b)]. The error was evaluated by taking into account the uncertainty in the molecular constants from the spectral simulation. Details of the molecular constants determined in this study are reported in a separate paper [58].

The predissociation spectra at longer storage times of 9.5–9.9 s and 195–200 s are shown in Figs. 4(c) and 4(d). The beam intensity in the ring decays with the storage time, and hence the neutral yield is shown after normalization to the bandhead intensity. The number of laser pulses per ion injection were 40 and 485 for Figs. 4(c) and 4(d), respectively. The spectra remain essentially the same shape within this time range due to the fact that the rotational RC lifetime is much longer than the timescale of the present experiment.

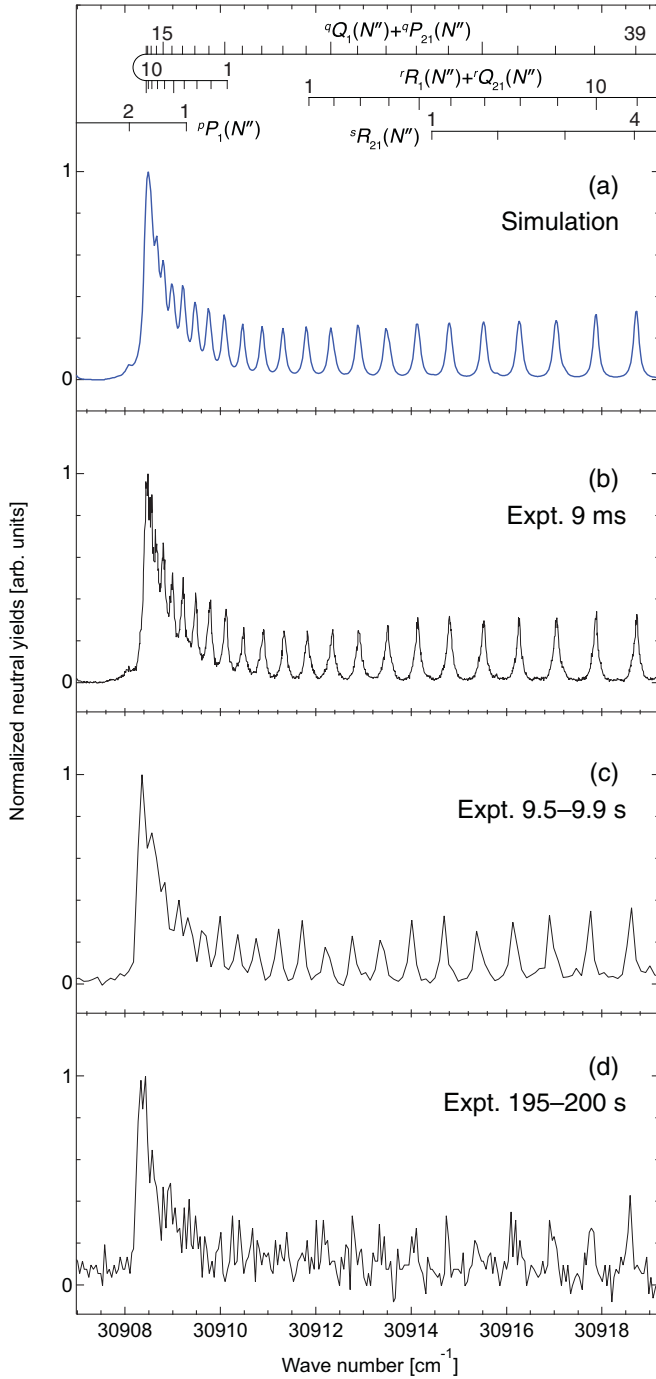


FIG. 4. Storage time dependence of the photodissociation spectrum in the main bandhead of $A^2\Sigma^+(2\ 0\ 0)-X^2\Pi_{3/2}(0\ 0\ 0)$. (a) The simulated spectrum assuming a rotational temperature of 320 K. The experimental spectra (b)–(d) were measured at storage times of 9 ms, 9.5–9.9 s, and 195–200 s, respectively. The assignment of the rotational structure is indicated in panel (a).

This behavior is qualitatively supported by our rotational RC simulation, as summarized in the Appendix.

B. Vibrational radiative cooling dynamics

Vibrational population evolution is described independently of the rotational RC process to an adequate approxi-

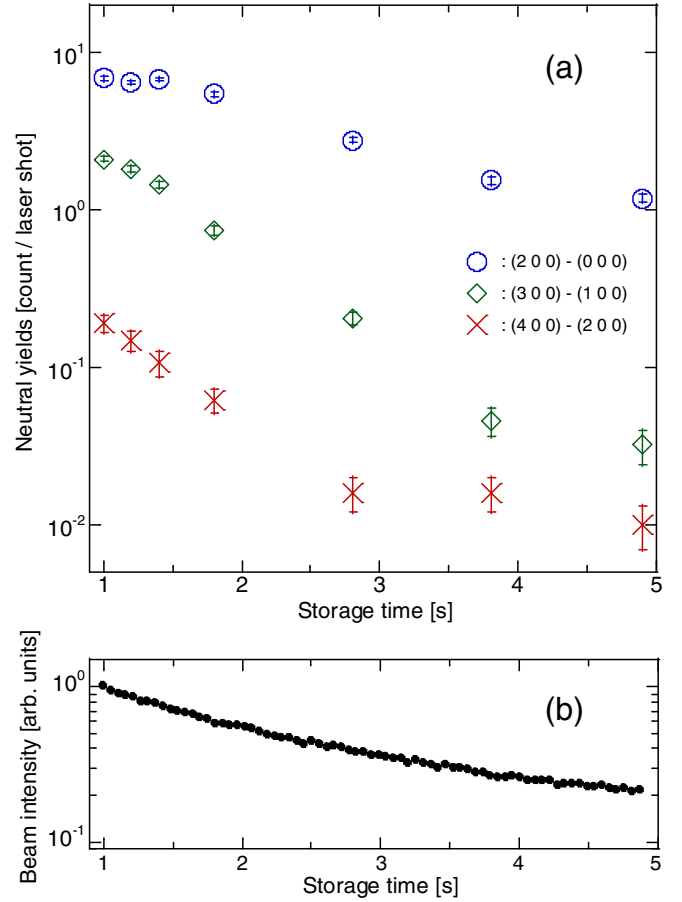


FIG. 5. (a) Neutral yields produced via laser-induced predissociation at each transition as a function of ion storage time before laser irradiation. The error bars represent the statistical error. (b) Storage time dependence of the neutral yields produced by ion-residual gas collisions, corresponding to the relative stored ion beam intensity.

mation. In general, the cooling behavior of rotational states is slower than vibrational cooling. We estimated the population evolution of the $X^2\Pi_{3/2}(0\ 0\ 0)$, $(1\ 0\ 0)$, and $(2\ 0\ 0)$ vibrational states from their spectral intensities at the bandheads indicated by the symbols in Fig. 3. The band-structure changes due to rotational radiative cooling are negligibly small during the time range of several seconds, which is verified by comparing spectra with different storage times up to 200 s, as demonstrated in Sec. III A. Thus, Fig. 5(a) shows the bandhead intensities observed at different storage times up to ≈ 5 s. For this storage time, neutral yields from residual-gas collisions were also recorded as a measure of the beam intensity in the ring for normalization [Fig. 5(b)]. In the time range earlier than 1 s, the rapid decrease of the neutral yields is not explained solely by collisions with residual gas or intrabeam collisions. These neutral yields do not correctly provide the number of stored ions on stable trajectories. Therefore, we only show storage times longer than 1 s.

The absolute population of each vibrational state was estimated from the bandhead intensities as shown in Fig. 6. Normalization of the populations required a three-step process. First, we took into account the normalization to the beam intensity after subtraction of laser-induced background. Second, the resulting populations are further

TABLE I. A list of wave number, wavelength, background, and relative predissociation probability $f_{\text{rel}}(v_1''00)$ [= $f_{\text{dis}}(v_1''00)/f_{\text{dis}}(000)$] for each observed transition. The laser wave number $\tilde{\nu}$ corresponds to the vibrational bandheads in the electronic transition $A^2\Sigma^+-X^2\Pi_{3/2}$ of N_2O^+ , and λ represents the corresponding wavelength in vacuum. The background of the neutral detectors was measured at each wavelength. $f_{\text{rel}}(v_1''00)$ represents the laser-induced dissociation probability for the $(v_1''00)$ populations with regards to the (000) ground-state population in $X^2\Pi_{3/2}$.

Transition ($v_1''00$)-($v_1''00$)	$\tilde{\nu}$ [cm^{-1}]	λ [nm]	Background [count/laser shot]	$f_{\text{rel}}(v_1''00)$
(2 0 0)-(0 0 0)	30908.4	323.54	2.5×10^{-3}	1
(3 0 0)-(1 0 0)	31105.6	321.49	8.5×10^{-3}	3.8
(4 0 0)-(2 0 0)	31311.5	319.37	1.5×10^{-2}	2.5

corrected by the relative predissociation probabilities $f_{\text{rel}}(v_1''00)$ [= $f_{\text{dis}}(v_1''00)/f_{\text{dis}}(000)$] for each transition ($v_1'' = 0, 1, 2$). The $f_{\text{dis}}(v_1''00)$ was obtained by multiplying the relative transition probability for each laser excitation and the branching ratio between the predissociation process and the deexcitation process to $X^2\Pi$. The former is estimated by using the Franck-Condon factor of each transition, as described in detail in the Appendix; for the latter, the reader is referred to the relevant literature [40]. We note that the observed (2 0 0) vibrational state is coupled with the (1 2 0) state via a Fermi resonance [26], and that this bandhead intensity is shared with the other bandhead coupled with the (2 0 0) and (1 2 0) states [48,58] according to the theoretical (2 0 0) composition of 0.55 [26]. Table I summarizes the laser wavelengths used, the corresponding wave numbers, the detector background, and $f_{\text{rel}}(v_1''00)$ for each transition. To compare these measured relative populations with the absolute simulation results, the photoexcitation cross section and the experimental conditions like the detector efficiency are needed, but they are practically difficult to obtain in the current experimental setup. Instead, to finally arrive at the absolute populations, the experimental values were further normalized to the value of the (0 0 0) state at 4.9 s storage time, because the (0 0 0) population will eventually reach 1.0 after sufficiently long storage times.

In Fig. 6, the (1 0 0) and (2 0 0) populations decrease with a decay constant of about 1 s^{-1} , whereas the (0 0 0) ground-state population does not show significant changes within this timescale. This implies that the initial populations of the vibrational excited states are relatively small. To understand this behavior, we performed a theoretical simulation on the cascade transition of vibrational RC processes. The simulation assumed two different conditions for the initial vibrational population distribution of N_2O^+ ions in the electronic ground state; the thermal-equilibrium model distribution of the Boltzmann type defined by a temperature T , and the nonequilibrium model distribution produced by Franck-Condon-type transitions from neutral N_2O . The thermal-equilibrium model assumes that the ions in the ECR plasma reach thermal equilibrium through multiple collision processes. Here, we adopted an initial temperature of 3000 K as a typical vibrational temperature in plasmas, referring to the vibrational temperature of N_2^+ in a laboratory plasma

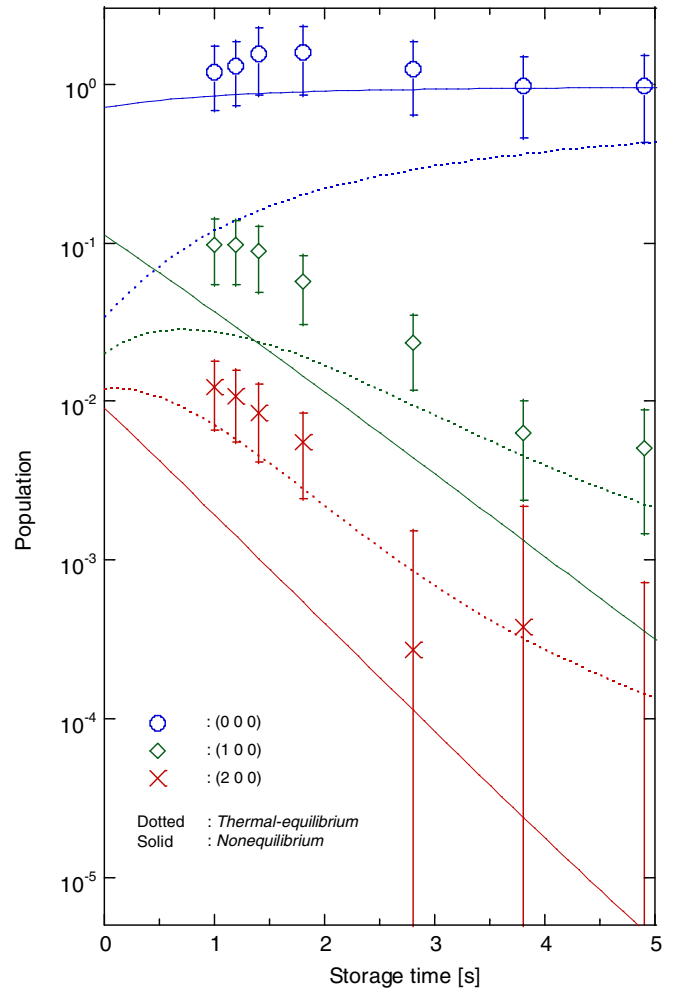


FIG. 6. Observed and simulated population evolutions for each vibrational state as a function of ion storage time. The dotted and solid lines represent simulation results under initial distributions in thermal equilibrium and nonequilibrium, respectively. The errors in the experimental values were determined by the uncertainty in the beam intensity, the statistical errors of the neutral yield and the subtracted background, and the propagation of the normalization error. The colors used correspond to the observed levels as shown in Fig. 5(a).

experiment [59]. The nonequilibrium model is based on the assumption that the ionic vibrational population distribution is determined by Franck-Condon transitions from neutral N_2O at room temperature and is not influenced by any collisions after ionization. The details of the simulation procedure are summarized in the Appendix. The results from the simulations are shown in Fig. 6 by dotted and solid lines for the thermal-equilibrium and nonequilibrium models, respectively. The vibrational relaxation process from the excited states (1 0 0) and (2 0 0) proceeds to the ground state through successive decays by $\Delta v_1 = 1$ transitions because the vibrational RC process for each mode develops independently reflecting the limited contribution of intermode transitions and Fermi resonances. Thus the simulated behavior shows that the population is depleted in order from the upper level. On the other hand, the population of the vibrational ground state (0 0 0) increase over time as a result of deexcitation from the higher excited

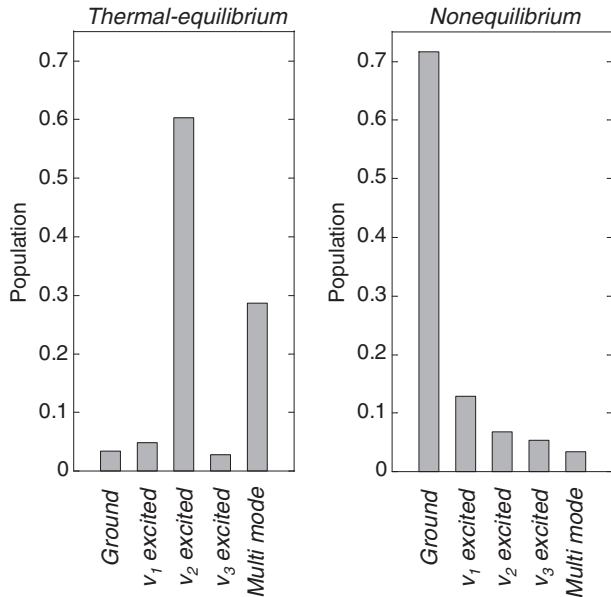


FIG. 7. The initial populations of ground, v_1 -, v_2 - and v_3 -excited, and multimode- excited states of N_2O^+ for the thermal-equilibrium and nonequilibrium models. Note that a sum of the populations in the excited states ($v_i = 1, 2, 3, \dots$) for each mode is shown.

states in all the vibrational modes. A comparison with the simulation indicates that our experimental results are reasonably explained by the nonequilibrium model assuming the initial population determined by the Franck-Condon principle. In particular, the plateau shape of the $(0\ 0\ 0)$ population strongly supports the nonequilibrium model rather than the thermal-equilibrium model. The decay rate of $(1\ 0\ 0)$ and $(2\ 0\ 0)$ population was also reproduced by the nonequilibrium model. We note that the experimental data for the $(1\ 0\ 0)$ and $(2\ 0\ 0)$ populations in Fig. 6 are considered to have some systematic errors related with the normalization procedure through the factor $f_{rel}(v_1''\ 0\ 0)$ in order to discuss the absolute population. One of the origins of these systematic errors is the uncertainty of the calculated predissociation probabilities [40]. Additionally, each bandhead is composed of unresolved rotational lines, and thus its spectral intensity depends on the rotational structure of the vibrational state; this is not considered in the present study. However, these issues only affect the normalization and not the relative temporal behavior of the vibrational states, i.e., the decay time profiles.

In the following, we discuss how the two models result in such significantly different behavior, which is crucial in understanding the dynamics of vibrational RC in molecules with multiple vibrational modes. In the present case, the key process governing the vibrational RC is the excitation of the v_2 bending mode. Compared with the v_1 and v_3 stretching modes, the v_2 mode has a smaller energy-level spacing and therefore a lower RC rate on the order of seconds. Therefore, the population of the v_2 excited state makes an obvious contribution to the slow increase in the $(0\ 0\ 0)$ population. Figure 7 shows the initial population distributions of each vibrational mode under the two initial conditions. Here, the excited states are categorized into single-mode (either v_1 , v_2 , or v_3) and multimode excited states. In the nonequilibrium model, more

than 70% of the N_2O^+ ions stay in the ground vibrational state $(0\ 0\ 0)$ from the beginning because the Franck-Condon factor to the vibrational ground state is significantly high due to the electronic structures of N_2O and N_2O^+ [40], and the v_2 mode is less populated. This reasonably explains the plateau behavior of the $(0\ 0\ 0)$ population in Fig. 6. On the other hand, in the thermal-equilibrium model, most of the ions are vibrationally excited and the highest population is found in the v_2 excited states. This high population of the v_2 state slowly decays into the $(0\ 0\ 0)$ state in the thermal-equilibrium model, making a significant difference in the behavior of the $(0\ 0\ 0)$ population in this time region. The initial population is also distributed to the multiple excited states $(1\ v_2\ 0)$ and $(2\ v_2\ 0)$ in the thermal-equilibrium distribution, which contribute to the transient increase of the $(1\ 0\ 0)$ and $(2\ 0\ 0)$ population within 1 s. Note that the RC simulation with the thermal-equilibrium model shows different behavior depending on the initial temperature. The plateau behavior of the $(0\ 0\ 0)$ state can also be reproduced by the thermal-equilibrium model by assuming an initial temperature as low as 300 K. However, in this case, the populations of $(1\ 0\ 0)$ and $(2\ 0\ 0)$ are suppressed by several orders of magnitude and do not match the experimental result. Therefore we conclude that the initial distribution of the stored ions obeys the nonequilibrium model.

This conclusion is relevant to the effective rotational temperature of 320 K determined in the previous section. The v_1 vibrational excited states observed in the experiment cannot be populated under the effective rotational temperature of 320 K, thus the ions injected into RICE did not satisfy thermal equilibrium. We further confirmed this from the time evolution of the population distribution of the vibrational state with multiple degrees of freedom because the population distribution in each mode reflects its specific character, as explained. Note that the behavior of the v_2 mode populations was not readily measured because of the relatively small intensities detected by action spectroscopy. In addition, the absolute population of each vibrational mode cannot be precisely evaluated by the spectral analysis due to the ambiguity of the dissociation probability.

IV. SUMMARY

The rovibrational RC processes of the triatomic N_2O^+ ion were studied by predissociation spectroscopy in the cryogenic electrostatic ion storage ring, RICE. High-resolution rovibrational spectra were obtained for 316–326 nm, in which the $A^2\Sigma^+-X^2\Pi$ transitions were observed for the $(2\ 0\ 0)$ - $(0\ 0\ 0)$, $(3\ 0\ 0)$ - $(1\ 0\ 0)$, and $(4\ 0\ 0)$ - $(2\ 0\ 0)$ vibrational bands. We estimated the rotational temperature of the N_2O^+ ions at 9 ms storage to be 320 K. This rotational population did not show any significant change at storage times up to 200 s, being consistent with the slow rotational RC rate attributed to the small electric-dipole moment and rotational constant of the N_2O^+ molecule. On the other hand, we clearly observed the RC behavior for the vibrationally excited states of $(1\ 0\ 0)$ and $(2\ 0\ 0)$ over a period of several seconds, while the noticeable increase of the population of the ground state $(0\ 0\ 0)$ was not observed. This behavior was reasonably reproduced by our RC simulation by assuming the initial vibrational distribution through Franck-Condon-type transitions rather than a Boltz-

mann distribution. The comparison between the experiment and the simulation demonstrated that the vibrational RC behavior of N_2O^+ strongly depends on the initial population distribution of multiple vibrational modes, especially since the energy-level spacings and resulting RC rates are different between these modes, and their interplay is negligibly small.

In summary, we found both vibrational cooling within 5 s and unchanged rotational behavior in the same molecule. This sharp imbalance between vibrational and rotational cooling, which has been well known both in theory and experiment, was clearly observed by the combination of long-time storage and high-precision spectroscopy. Furthermore, the cooling dynamics were traced in real time and revealed the relevant mechanism inside. These dynamics in a simple system such as triatomic molecules are essential as a fundamental aspect of understanding nonthermal and nonequilibrium behavior.

ACKNOWLEDGMENTS

We would like to thank Prof. E. J. Bieske of The University of Melbourne and Prof. M. Hoshino of Sophia University for helpful suggestions and discussions. This work was supported by the RIKEN Basic Science Interdisciplinary Research Projects, Yamada Science Foundation and by the JSPS KAKENHI Grants No. 26220607, No. 16K13859, No. 17H02993, No. 18H03714, No. 19H05195, and No. 20K20110.

APPENDIX A: ROTATIONAL AND VIBRATIONAL RADIATIVE COOLING SIMULATIONS

To discuss the observed RC dynamics, we constructed a simulation program for the level population evolution based on a simple cascade model. We considered rotational and vibrational RC separately. Both are regarded to proceed through spontaneous deexcitation from the upper levels.

1. Rotational radiative cooling simulation

Regarding rotations, the linear triatomic molecule N_2O^+ has two degrees of freedom, corresponding to rotation about the two orthogonal axes perpendicular to the symmetry axis.

The A coefficients of the allowed rotational transitions with $\Delta J = \pm 1, 0$ were calculated by using PGOPHER [57].

For the rotational RC simulations, excitation due to black-body radiation (BBR) was taken into account. The B coefficient is derived by the relation between the Einstein A and B coefficients, $A = \frac{8\pi h\nu^3}{c^3} B$ (h is Planck's constant, c is the speed of light), and the radiation density $\rho(\nu_{ij})$ for photons with energy $h\nu_{ij}$ (for the transition between states i and j) is given by Planck's law assuming an environmental temperature of 4 K.

When we define the population of $N_R(t)$, and $A_{i,j}$ and $B_{i,j}$ between the state i and j , the rate equation for a rotationally excited level i under spontaneous emission, induced emission and induced absorption, is given by

$$\begin{aligned} \frac{dN_R(t)}{dt} = & A_{i,i+1}N_{i+1}(t) - A_{i-1,i}N_i(t) \\ & + B_{i,i+1}\rho(\nu_{i,i+1})N_{i+1}(t) - B_{i-1,i}\rho(\nu_{i-1,i})N_i(t) \\ & + B_{i,i-1}\rho(\nu_{i,i-1})N_{i-1}(t) - B_{i+1,i}\rho(\nu_{i+1,i})N_i(t). \end{aligned} \quad (\text{A1})$$

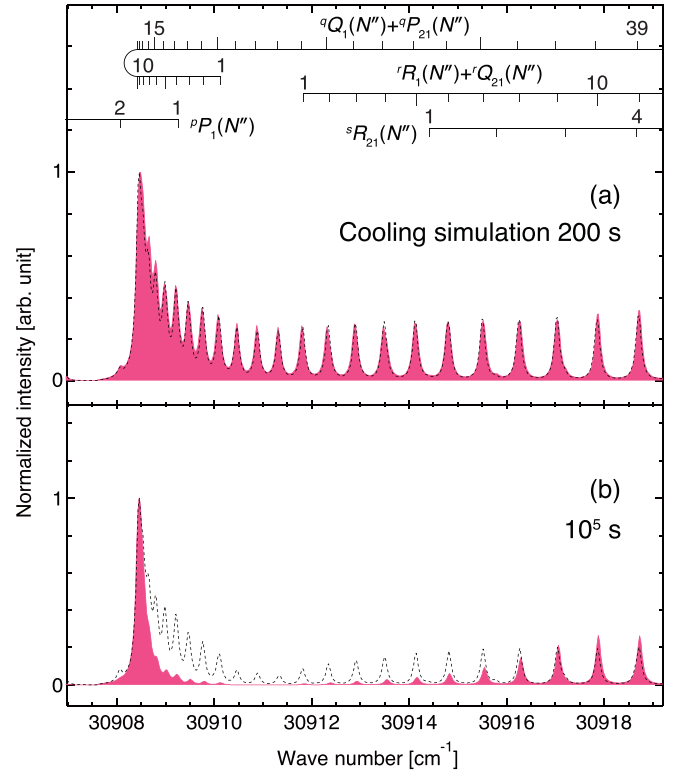


FIG. 8. Results of the rotational RC simulation with an initial rotational temperature of 400 K. The spectra (filled with pink) were constructed from the simulated rotational population at storage times of (a) 200 s, and (b) 10^5 s. The dashed curves in panels (a) and (b) represent the spectra using Boltzmann distributions at 400 and 120 K, respectively.

We traced the evolution of the population by numerically solving the above rate equation under the initial condition of a specific rotational temperature. In the present simulation, we considered all rotational states with $j < 100$. Figure 8 shows the spectra constructed from the simulated rotational population under initial temperature of 400 K. As shown in Fig. 8(a), the simulation spectrum at 200 s is unchanged and is well reproduced by a Boltzmann distribution under the initial effective temperature. The small rotational spontaneous emission rates of N_2O^+ require a long storage time to exhibit a significant population change. It is clearly shown for 10^5 s storage in Fig. 8(b). The obtained spectrum cannot be described by a Boltzmann distribution; for instance, when we assumed an effective temperature of 120 K so that the highest population level with a Boltzmann distribution may coincide with the observed spectrum, the population of the lower rotational levels largely deviated from the simulated spectrum.

2. Vibrational radiative cooling simulation

As previously discussed, N_2O^+ has three vibrational modes: a NN-O stretching mode (ν_1), a bending mode (ν_2), and a N-NO stretching mode (ν_3). The bending mode is doubly degenerate, and the combination of these vibrations produces the angular momentum along the molecular axis.

TABLE II. Frequencies and anharmonic terms of vibrational modes of N_2O^+ [cm^{-1}] [54].

ω_1	ω_2	ω_3	x_{11}	x_{13}	x_{12}	x_{33}	g
1138.29	452.28	1756.8	-14.16	13.69	-4.81	-21.58	3.05

This vibrational angular momentum is represented by l . Hereafter we denote the vibrational state of N_2O^+ as $(v_1 v_2^l v_3)$.

The vibrational term $G(v_1 v_2^l v_3)$ including the anharmonic term can be written as follows:

$$\begin{aligned}
 G(v_1 v_2^l v_3) = & \omega_1 \left(v_1 + \frac{1}{2} \right) + \omega_2 (v_2 + 1) + \omega_3 \left(v_3 + \frac{1}{2} \right) \\
 & + x_{11} \left(v_1 + \frac{1}{2} \right)^2 + x_{22} (v_2 + 1)^2 \\
 & + x_{33} \left(v_3 + \frac{1}{2} \right)^2 + x_{12} \left(v_1 + \frac{1}{2} \right) (v_2 + 1) \\
 & + x_{13} \left(v_1 + \frac{1}{2} \right) \left(v_3 + \frac{1}{2} \right) \\
 & + x_{23} (v_2 + 1) \left(v_3 + \frac{1}{2} \right) + gl^2. \quad (\text{A2})
 \end{aligned}$$

Note that the reported experimental values listed in Table II are employed for the frequency and the coefficient of the anharmonic term. The values of x_{23} and x_{22} have not been determined experimentally, but were calculated by Gritli *et al.* [26] to be -0.7543 and -0.6902 cm^{-1} , respectively. However, we assumed $x_{23}, x_{22} = 0$, partly because deviations of about $\pm 1 \text{ cm}^{-1}$ often exist between experiment and theory for the anharmonic term, and partly because they are close to zero and thus have little effect on the results.

When the ground state is used as an energy reference, the state energy E_v is given by

$$E_v(v_1 v_2^l v_3) = G(v_1 v_2^l v_3) - G(000). \quad (\text{A3})$$

Using Eq. (A2), the vibrational ground-state term $G(000)$ is calculated to be 1891.908 cm^{-1} . Thus, the transition energies between the states are obtained for all transitions considered in accordance with the selection rules $\Delta v = 1, \Delta l = 1$.

The A coefficients of the vibrational transitions were calculated by Gaussian 09 [60] using the B3LYP method with the aug-cc-pVDZ basis set. We obtained two different values for the frequency and the intensity in the degenerate v_2 bending mode, indicating the Renner-Teller splitting in the Π electronic nature of the ground state X . We adopted the larger intensity for simplicity. The A coefficient for each vibration mode is given by

$$A_{v_1} = \frac{8\pi v}{\lambda^2} S_{v_1}, \quad A_{v_2} = \frac{8\pi(v \mp l)}{\lambda^2} S_{v_2}, \quad A_{v_3} = \frac{8\pi v}{\lambda^2} S_{v_3}. \quad (\text{A4})$$

Here, λ and S_{v_n} represent the wavelength of the transition and the band intensity for the fundamental transitions, respectively. v and l represent the vibrational quantum number and the vibrational angular momentum of the upper level. Note that we employ the reported transition frequencies from experiments [54] for use in Eqs. (A2) and (A3), not from

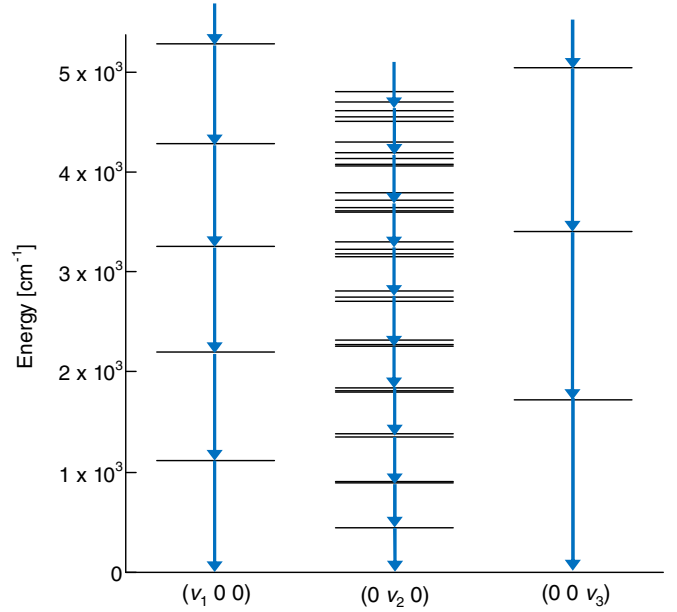


FIG. 9. Schematic energy levels of three vibrational modes of N_2O^+ .

our calculation by the Gaussian code, because the former are considered to be more precise. Figure 9 shows the vibrational energy levels except for multimode-excited states. We employ the calculated value obtained with the Gaussian code for S_{v_n} . As an example, the obtained A coefficients for the fundamental transition of each mode are summarized in Table III, and the other transitions related to higher states were treated in the same manner.

In this case, excitation due to BBR was not taken into account because the energy of the first vibrational excited level is significantly larger than the BBR at 4 K. Also, the intermode transition (IMT) probability between different vibrational modes is negligibly small, and thus we ignored this contribution. These are schematically shown in Fig. 9. Therefore, when we define the population of the state $(v_1 v_2 v_3) = (i j k)$ as $N_{i,j,k}(t)$, and $A_{i,i'}$ as the A coefficient for each transition, the rate equation for a vibrationally excited level $(i j^l k)$ under spontaneous emission is simply given by

$$\begin{aligned}
 \frac{dN_{i,j^l,k}(t)}{dt} = & A_{i,i+1} N_{i+1,j^l,k}(t) \\
 & - A_{i-1,i} N_{i,j^l,k}(t) \\
 & + A_{j^l,j+1^{l-1}} N_{i,j+1^{l-1},k}(t) \\
 & - A_{j-1^{l-1},j^l} N_{i,j^l,k}(t) \\
 & + A_{j^l,j+1^{l+1}} N_{i,j+1^{l+1},k}(t) \\
 & - A_{j-1^{l+1},j^l} N_{i,j^l,k}(t) \\
 & + A_{k,k+1} N_{i,j^l,k+1}(t) \\
 & - A_{k-1,k} N_{i,j^l,k}(t). \quad (\text{A5})
 \end{aligned}$$

Here, the population falling into the state of $\Delta v = -1$ and that of falling from the state of $\Delta v = +1$ due to spontaneous

TABLE III. Calculated A coefficient for the fundamental transition of each mode.

	Transition	A [s^{-1}]
Mode 1	(1 0 0)-(0 0 0)	1.31
Mode 2	(0 1 0)-(0 0 0)	0.30
Mode 3	(0 0 1)-(0 0 0)	0.94

emission are taken into account. In the bending mode v_2 , the transitions with the vibrational angular momentum $\Delta l = \pm 1$ were also included. Once the initial distribution and the A coefficients are determined, the level population at an arbitrary time can be obtained. We took into account the states up to $(v_1 v_2^l v_3) = (10 0 0)$, $(0 10^{10} 0)$, $(0 0 6)$, and multimode-excited states where two vibration modes are actively excited simultaneously like $(1 2 0)$ are considered up to $(2 2 2)$. We treated the levels whose relative population is larger than 1% of the whole.

We do not include contributions from overtone transitions; however, Fermi resonances were considered. The resulting resonance levels and their intensities have been reported [26], and we included them into the calculation by using the values listed in Table IV for the corresponding states, with each state being expressed as the sum of its constituting states. For example, the $(1 1 0)^2 \Delta_{5/2}$ and $(0 3 0)\kappa^2 \Delta_{5/2}$ states are considered by coupling the $(1 1 0)$ and $(0 3 0)\kappa$ states, as shown in the last two columns of Table IV. The state marked with κ represents the higher-energy component of the states split by the Renner-Teller effect. As already mentioned, we replaced two different bending modes by double counting of one specific mode with a larger amplitude, which corresponds to the higher-energy component in the present case. This may lead to overestimation to some extent for the decay rates; however, the overall contribution to the cascade is small.

For the Fermi resonances, the populations of the coupled states were regarded as the sum of the constituting component populations with the configuration weight summarized in Table IV. The transitions of the constituting components were separately treated, and the transition rates were also weighted.

TABLE IV. Vibronic levels in the Fermi resonances of N_2O^+ .

Level	Energy [cm^{-1}]	Configuration
$(0 4 0)\kappa^2 \Pi_{3/2}$	2066.90	0.93 $(0 4 0)\kappa$, 0.05 $(1 2 0)\kappa$
$(2 0 0)^2 \Pi_{3/2}$	2210.82	0.55 $(2 0 0)$, 0.42 $(1 2 0)\kappa$
$(1 2 0)\kappa^2 \Pi_{3/2}$	2235.78	0.52 $(1 2 0)\kappa$, 0.45 $(2 0 0)$
$(1 1 0)^2 \Delta_{5/2}$	1558.70	0.71 $(1 1 0)$, 0.28 $(0 3 0)\kappa$
$(0 3 0)\kappa^2 \Delta_{5/2}$	1588.41	0.71 $(0 3 0)\kappa$, 0.28 $(1 1 0)$

APPENDIX B: THE INITIAL VIBRATIONAL POPULATION OF N_2O^+ THROUGH FRANCK-CONDON-TYPE TRANSITIONS FROM THE NEUTRAL BY ELECTRON IMPACT

We performed a simulation by assuming the initial population of ions produced by electron impact, where transitions obeying the Franck-Condon factors (FCFs) hold. When we assume that the vibrational motions are independent of the electronic degrees of freedom upon ionization by collisions with electrons in the plasma source, the FCFs determine the vibrational population of the produced ions. In the FCF calculation, we adopted a simple model used by Tokue *et al.* [40], which successfully explains the intensity ratios of the A - X fluorescence spectrum of N_2O^+ produced by electron impact of N_2O . The degeneracy of the bending mode was included by doubling the population of this mode in the calculation. The neutral N_2O in its ground state and the cation N_2O^+ in the X and A states have linear configurations (C_∞). Following the treatment in the relevant paper [40], we approximated the neutral and the ion with the $D_{\infty h}$ symmetry and ignore the Duschinsky effect that describes the rotation of the normal coordinates in the transitions [61]. The three independent harmonic oscillators were used as the vibrational wave functions whose frequencies were taken from Ref. [40]. The ionization branching ratio to the ionic ground state X and the rest to the excited state A by electron collision is not known. Here, we simply assumed an approximate ratio of 1 : 1, according to the results of photoelectron spectroscopy [62]. Then, according to the fluorescence quantum yields summarized in Ref. [40], this population was redistributed to the vibrational levels in the ground state. The fluorescence yields of the levels that are not referred to in Ref. [40] were taken to be null.

- [1] R. C. Dunbar, *Mass Spectrom. Rev.* **11**, 309 (1992).
 [2] H. T. Schmidt, *Phys. Scr.* **166**, 014063 (2015).
 [3] H. Kreckel, J. Tennyson, D. Schwalm, D. Zajfman, and A. Wolf, *New J. Phys.* **6**, 151 (2004).
 [4] M. Larsson, *Philos. Trans. R. Soc., A* **370**, 5118 (2012).
 [5] Z. Amitay, A. Bear, M. Dahan, L. Knoll, M. Lange, J. Levin, I. F. Schneider, D. Schwalm, A. Suzor-Weiner, Z. Vager *et al.*, *Science* **281**, 75 (1998).
 [6] M. Goto, A. E. K. Sundén, H. Shiromaru, J. Matsumoto, H. Tanuma, T. Azuma, and K. Hansen, *J. Chem. Phys.* **139**, 054306 (2013).
 [7] K. Najafian, M. S. Pettersson, B. Dynefors, H. Shiromaru, J. Matsumoto, H. Tanuma, T. Furukawa, T. Azuma, and K. Hansen, *J. Chem. Phys.* **140**, 104311 (2014).
 [8] N. Kono, T. Furukawa, H. Tanuma, J. Matsumoto, H. Shiromaru, T. Azuma, K. Najafian, M. S. Pettersson, B. Dynefors, and K. Hansen, *Phys. Chem. Chem. Phys.* **17**, 24732 (2015).
 [9] G. Ito, T. Furukawa, H. Tanuma, J. Matsumoto, H. Shiromaru, T. Majima, M. Goto, T. Azuma, and K. Hansen, *Phys. Rev. Lett.* **112**, 183001 (2014).
 [10] V. Chandrasekaran, B. Kafle, A. Prabhakaran, O. Heber, M. Rappaport, H. Rubinstein, D. Schwalm, Y. Toker, and D. Zajfman, *J. Phys. Chem. Lett.* **5**, 4078 (2014).

- [11] S. Martin, J. Bernard, R. Brédy, B. Concina, C. Joblin, M. Ji, C. Ortega, and L. Chen, *Phys. Rev. Lett.* **110**, 063003 (2013).
- [12] S. Martin, J. Matsumoto, N. Kono, M.-C. Ji, R. Brédy, J. Bernard, A. Cassimi, and L. Chen, *Nucl. Instrum. Methods Phys. Res., Sect. B* **408**, 209 (2017).
- [13] K. Hansen, *Statistical Physics of Nanoparticles in the Gas Phase*, 2nd ed. (Springer, Dordrecht, 2018).
- [14] C. Breitenfeldt, K. Blaum, S. George, J. Göck, G. Guzmán-Ramírez, J. Karthein, T. Kolling, M. Lange, S. Menk, C. Meyer *et al.*, *Phys. Rev. Lett.* **120**, 253001 (2018).
- [15] S. Martin, M. Ji, J. Bernard, R. Brédy, B. Concina, A. R. Allouche, C. Joblin, C. Ortega, G. Montagne, A. Cassimi, Y. Ngonon-Ravache, and L. Chen, *Phys. Rev. A* **92**, 053425 (2015).
- [16] H. T. Schmidt, R. D. Thomas, M. Gatchell, S. Rosén, P. Reinhard, P. Löfgren, L. Brännholm, M. Blom, M. Björkhage, E. Bäckström *et al.*, *Rev. Sci. Instrum.* **84**, 055115 (2013).
- [17] R. von Hahn, A. Becker, F. Berg, K. Blaum, C. Breitenfeldt, H. Fadil, F. Fellenberger, M. Froese, S. George, J. Göck *et al.*, *Rev. Sci. Instrum.* **87**, 063115 (2016).
- [18] Y. Nakano, Y. Enomoto, T. Masunaga, S. Menk, P. Bertier, and T. Azuma, *Rev. Sci. Instrum.* **88**, 033110 (2017).
- [19] J. N. Bull, M. S. Scholz, E. Carrascosa, M. K. Kristiansson, G. Eklund, N. Punnakayathil, N. de Ruelle, H. Zettergren, H. T. Schmidt, H. Cederquist, and M. H. Stockett, *J. Chem. Phys.* **151**, 114304 (2019).
- [20] K. Hansen, M. H. Stockett, M. Kamińska, R. F. Nascimento, E. K. Anderson, M. Gatchell, K. C. Chartkunchand, G. Eklund, H. Zettergren, H. T. Schmidt, and H. Cederquist, *Phys. Rev. A* **95**, 022511 (2017).
- [21] E. K. Anderson, M. Kamińska, K. C. Chartkunchand, G. Eklund, M. Gatchell, K. Hansen, H. Zettergren, H. Cederquist, and H. T. Schmidt, *Phys. Rev. A* **98**, 022705 (2018).
- [22] A. P. O'Connor, A. Becker, K. Blaum, C. Breitenfeldt, S. George, J. Göck, M. Grieser, F. Grussie, E. A. Guerin, R. von Hahn *et al.*, *Phys. Rev. Lett.* **116**, 113002 (2016).
- [23] C. Meyer, A. Becker, K. Blaum, C. Breitenfeldt, S. George, J. Göck, M. Grieser, F. Grussie, E. A. Guerin, R. von Hahn *et al.*, *Phys. Rev. Lett.* **119**, 023202 (2017).
- [24] O. Novotný, P. Wilhelm, D. Paul, Á. Kálosi, S. Saurabh, A. Becker, K. Blaum, S. George, J. Göck, M. Grieser *et al.*, *Science* **365**, 676 (2019).
- [25] H. T. Schmidt, G. Eklund, K. C. Chartkunchand, E. K. Anderson, M. Kamińska, N. de Ruelle, R. D. Thomas, M. K. Kristiansson, M. Gatchell, P. Reinhard *et al.*, *Phys. Rev. Lett.* **119**, 073001 (2017).
- [26] H. Gritli, Z. B. Lakhdar, G. Chambaud, and P. Rosmus, *Chem. Phys.* **178**, 223 (1993).
- [27] B. Brocklehurst, *Nature (London)* **182**, 1366 (1958).
- [28] J. Lermé, S. Abed, R. A. Holt, M. Larzilliere, and M. Carré, *Chem. Phys. Lett.* **96**, 403 (1983).
- [29] J. Lermé, S. Abed, R. A. Holt, M. Larzilliere, and M. Carré, *J. Chem. Phys.* **84**, 2167 (1986).
- [30] M. Larzillière, K. Gragued, J. Lermé, and J. Brocke Koffend, *Chem. Phys. Lett.* **134**, 467 (1987).
- [31] S. Abed, M. Broyer, M. Carré, M. L. Gaillard, and M. Larzillière, *Chem. Phys.* **74**, 97 (1983).
- [32] M. Larzillière and Ch. Jungen, *Mol. Phys.* **67**, 807 (1989).
- [33] M. Chafik el Idrissi, M. Larzilliere, and M. Carré, *J. Chem. Phys.* **100**, 204 (1994).
- [34] R. Frey, R. Kakoschke, and E. W. Schlag, *Chem. Phys. Lett.* **93**, 227 (1982).
- [35] J. H. Callomon and F. Creutzberg, *Phil. Trans. R. Soc. London A* **277**, 157 (1974).
- [36] J. P. Maier and F. Thommen, *Chem. Phys.* **51**, 319 (1980).
- [37] J. A. Beswick and M. Horani, *Chem. Phys. Lett.* **78**, 4 (1981).
- [38] D. Klapstein and J. P. Maier, *Chem. Phys. Lett.* **83**, 590 (1981).
- [39] G. Kindvall, M. Larsson, B. Olsson, and P. Siggray, *Phys. Scr.* **33**, 412 (1986).
- [40] I. Tokue, M. Kobayashi, and Y. Ito, *J. Chem. Phys.* **96**, 7458 (1992).
- [41] J. W. Duff and D. R. Smith, *J. Atmos. Sol.-Terr. Phys.* **62**, 1199 (2000).
- [42] M. Richard-Viard, O. Atabek, O. Dutuit, and P. M. Guyon, *J. Chem. Phys.* **93**, 8881 (1990).
- [43] N. Komiha, *J. Mol. Struct.: THEOCHEM* **306**, 313 (1994).
- [44] G. Chambaud, H. Gritli, P. Rosmus, H.-J. Werner, and P. J. Knowles, *Mol. Phys.* **98**, 1793 (2000).
- [45] H. Wang, X. Zhou, S. Liu, B. Jiang, D. Dai, and X. Yang, *J. Chem. Phys.* **132**, 244309 (2010).
- [46] Q. Meng, H. Chang, M.-B. Huang, and H. Dong, *Theor. Chem. Acta* **128**, 359 (2011).
- [47] H. Xu, Y. Guo, Q. Li, Y. Shi, S. Liu, and X. Ma, *J. Chem. Phys.* **121**, 3069 (2004).
- [48] C. E. Fellows and M. Vervloet, *Chem. Phys.* **264**, 203 (2001).
- [49] C. E. Fellows, *J. Chem. Phys.* **138**, 164316 (2013).
- [50] L. L. Lessa, S. D. Cândido, and C. E. Fellows, *J. Chem. Phys.* **140**, 214311 (2014).
- [51] J. D. Burley, K. M. Ervin, and P. B. Armentrout, *J. Chem. Phys.* **86**, 1944 (1987).
- [52] B. Zolesi and L. R. Cander, *The General Structure of the Ionosphere in Ionospheric Prediction and Forecasting* (Springer, Berlin, Heidelberg, 2014).
- [53] M. J. Deluca and M. A. Johnson, *Chem. Phys. Lett.* **162**, 255 (1989).
- [54] M. A. Gharaibeh and D. J. Clouthier, *J. Chem. Phys.* **136**, 044318 (2012).
- [55] A. Dzhonson, D. Gerlich, E. J. Bieske, and J. P. Maier, *J. Mol. Struct.* **765**, 93 (2006).
- [56] Y. Nakano, R. Igosawa, S. Iida, S. Okada, M. Lindley, S. Menk, R. Nagaoka, T. Hashimoto, S. Yamada, T. Yamaguchi, S. Kuma, and T. Azuma, [arXiv:2004.03711](https://arxiv.org/abs/2004.03711).
- [57] C. M. Western, *J. Quant. Spectrosc. Radiat. Transf.* **186**, 221 (2017).
- [58] R. Igosawa, A. Hirota, N. Kimura, S. Kuma, K. C. Chartkunchand, P. M. Mishra, M. Lindley, T. Yamaguchi, Y. Nakano, and T. Azuma (unpublished).
- [59] F. D. Nascimento, S. Moshkalev, and M. Machida, *Contribut. Plasma Phys.* **1** (2020), doi: 10.1002/ctpp.201900046.
- [60] Gaussian 09, Revision E.01, M. J. Frisch *et al.*, Gaussian Inc., Wallingford CT (2016).
- [61] F. T. Chau, *J. Mol. Struct.: THEOCHEM* **151**, 157 (1987).
- [62] *Molecular Photoelectron Spectra and Ions States*, edited by K. Kimura (Japan Scientific Societies Press., 1995), in Japanese.